Incorporation of Mn in $Al_xGa_{1-x}N$ probed by x-ray absorption and emission spectroscopy, high-resolution microscopy, x-ray diffraction, and first-principles calculations

Mauro Rovezzi,[1,*] Wolfgang Schlögelhofer,[1,2] Thibaut Devillers,[2] Nevill Gonzalez Szwacki,[3] Tian Li,[4] Rajdeep Adhikari,[2] Pieter Glatzel,[1] and Alberta Bonanni[2,†]

[1]*European Synchrotron Radiation Facility, 71 Avenue des Martyrs, CS 40220 Grenoble, France*
[2]*Institute of Semiconductor and Solid State Physics, Johannes Kepler University, Altenberger Straße 69, A-4040 Linz, Austria*
[3]*Institute of Theoretical Physics, Faculty of Physics, University of Warsaw, ul. Pasteura 5, PL-02-093 Warszawa, Poland*
[4]*Institute of Physics, Polish Academy of Sciences, Al. Lotników 32/46, PL-02-668 Warszawa, Poland*

Synchrotron radiation x-ray absorption and emission spectroscopy techniques, complemented by high-resolution transmission electron microscopy methods and density functional theory calculations, are employed to investigate the effect of Mn in $Al_xGa_{1-x}N$:Mn samples with an Al content up to 100%. The atomic and electronic structure of Mn is established together with its local environment and valence state. A dilute alloy without precipitation is obtained for $Al_xGa_{1-x}N$:Mn with Al concentrations up to 82%, and the surfactant role of Mn in the epitaxial process is confirmed.

PACS number(s): 81.05.Ea, 61.05.cj, 78.70.En, 68.55.Ln

I. INTRODUCTION

Heterostructures based on group-III nitrides [1] and in particular on the combination $Al_xGa_{1-x}N$/GaN represent the basis of a variety of state-of-the-art (opto)electronic devices such as blue and white light-emitting diodes [2], laser diodes [3], blue lasers [4], and high-power [5] and high-electron-mobility transistors [6]. Most of the above mentioned devices are commercially available and their performance is continuously improved. Furthermore, group-III nitrides doped with transition metals (TM) have also been the focus of considerable research efforts towards the demonstration of semiconductor spintronic functionalities [7]. In this respect, while a remarkable number of reports on GaN:Mn provide an overview of the structural, optical, magnetic, and electric properties of this material system [8–15], little is known about $Al_xGa_{1-x}N$:Mn [16–19] and related nanostructures [20]. Recent findings [21] indicate this alloy to be particularly interesting for, e.g., the self-assembling of functional multilayers and for having revealed the decisive role of Mn as surfactant during the epitaxial growth of $Al_xGa_{1-x}N$:Mn, considerably enhancing the critical thickness of $Al_xGa_{1-x}N$:Mn on GaN, and opening new perspectives for the realization of, e.g., improved reflectors in GaN-based laser structures. We report here on $Al_xGa_{1-x}N$:Mn grown by means of metalorganic vapor phase epitaxy (MOVPE) in a broad range of Al concentrations and extensively investigated via x-ray absorption spectroscopy (XAS), x-ray emission spectroscopy (XES), energy-dispersive spectrometry (EDS), x-ray diffraction (XRD), and high-resolution (HR) transmission electron microscopy (TEM), supported by density functional theory (DFT) calculations. The results provide fundamental information on the microstructure and local environment in the layers and on the valence state of Mn incorporated in the lattice over the whole range of Al concentrations.

II. EXPERIMENTAL AND THEORETICAL METHODS

The wurtzite $Al_xGa_{1-x}N$:Mn samples are grown in an AIXTRON 200RF horizontal-tube MOVPE reactor. All structures are deposited on *c*-plane sapphire substrates with trimethylgallium (TMGa), trimethylaluminum (TMAl), bis-methylcyclopentadienyl-manganese (MeCp$_2$Mn), and ammonia (NH$_3$) as precursors for respectively Ga, Al, Mn, and N, with H$_2$ as carrier gas. The epitaxial process, developed from a well established procedure [22], consists of (i) substrate nitridation; (ii) low temperature (540 °C) deposition of a GaN nucleation layer (NL); (iii) its annealing under NH$_3$; (iv) growth of a 1 μm device-quality GaN buffer deposited at 1020 °C; (v) $Al_xGa_{1-x}N$:Mn layers at 850 °C, with the same TMGa and MeCp$_2$Mn flow rates and different—over the sample series—TMAl flow rates ranging from 1 to 80 standard cubic centimeters per minute (sccm). In order to have real time control over the entire fabrication process, the MOVPE system is equipped with an *in situ* Isa Jobin Yvon ellipsometer that allows for both spectroscopic and kinetic measurements in the energy range 1.5–5.5 eV [23]. The structures are routinely characterized by atomic force microscopy (AFM), secondary-ion mass spectroscopy (SIMS), and (magneto)photoluminescence (PL) in order to get information on the surface roughness, chemical composition, and magneto-optical response, respectively. Measurements of superconducting quantum interference device (SQUID) magnetometry, in the temperature range between 1.5 K and room temperature, confirm the samples to be paramagnetic. Here, we focus on the effect of Mn incorporation on the structural arrangement of $Al_xGa_{1-x}N$:Mn and on the local atomic environment of Mn, with particular attention to the XRD and HRTEM analysis as essential complement to the synchrotron XAS and XES measurements. All considered $Al_xGa_{1-x}N$:Mn samples are listed together with their growth parameters in Table I. The Mn concentration in all doped layers is $\approx$1% cations, as established by SIMS analysis. High resolution XRD measurements are carried out in a PANalytical's X'Pert PRO Materials Research Diffractometer (MRD) equipped with a hybrid monochromator (parabolic-shaped multilayer mirror

*mauro.rovezzi@esrf.eu
†alberta.bonanni@jku.at

TABLE I. Growth parameters for the $Al_xGa_{1-x}N$:Mn samples presented in this work. Al concentration x (from XRD); TMGa and TMAl flow rates and the pressure P in the reactor during the process. The $MeCp_2Mn$ and NH_3 flow rates are fixed at 490 sccm and 1500 sccm, respectively; the substrate temperature during the growth of the GaN buffer layer and during the deposition of the $Al_xGa_{1-x}N$:Mn layer are, respectively, 1020 °C and 850 °C. The nominal thickness is obtained from the kinetic ellipsometry spectra and confirmed by TEM cross sections.

Sample	x (%)	TMGa (sccm)	TMAl (sccm)	P (mbar)	Thickness (nm)
#A	0	1	0	200	500
#B	12	1	1	100	260
#C	20	1	3	100	293
#D	41	1	9	100	377
#E	59	1	27	100	553
#F	71	1	80	100	845
#G	82	1	80	50	780
#H	100	0	80	100	553

and a channel-cut Ge crystal) and a $1/4°$ divergence slit. The diffracted beam is measured with a solid-state PixCel detector used as a 256-channels detector with a 11.9 mm antiscatter slit. For the whole series of $Al_xGa_{1-x}N$:Mn samples, θ-2θ scans are acquired for 2θ values between 30° and 80° and complemented with maps of asymmetric diffraction peaks. These measurements provide information on the composition and strain state of the films [24].

Cross-sectional TEM specimen are prepared by mechanical polishing, dimpling, and final ion milling in a Gatan Precision Ion Polishing System. The samples are studied using both conventional and scanning transmission electron microscopy (CTEM/STEM) for bright/dark-field (BF/DF), HRTEM, and high angle annular dark-field (HAADF) imaging. The EDS technique is employed to analyze the chemical distribution of the various elements in the samples. The measurements reported here are performed in a FEI Titan Cube 80-300 operating at 300 keV, while a JEOL 2010F operating at 200 keV is routinely employed for preliminary characterization of all the grown samples.

The x-ray absorption and emission measurements at the Mn K edge (6539 eV) are carried out at the beamline ID26 of the European Synchrotron Radiation Facility (ESRF). The incoming x-ray beam, linearly polarized in the horizontal plane, is produced by three coupled undulators (u35) and monochromatized using a cryogenically cooled double Si(111) crystal monochromator. Harmonics rejection and heat load removal are achieved by using three Si mirrors at glancing angle of 2.5 mrad. The beam focusing (horizontal and vertical) is performed by means of two Si bent mirrors. This configuration permits us to obtain a beam size of $\approx(600\times100)$ μm^2 (horizontal × vertical) and a flux of $\approx10^{13}$ ph/s on the sample. The measurements are carried out in fluorescence mode at room temperature and under nitrogen flow to avoid depositing ambient impurities on the samples' surface. The total fluorescence yield (TFY) spectra are obtained with a Si photodiode, while the high energy resolution fluorescence detected (HERFD) spectra are acquired with a wavelength

dispersive spectrometer equipped with five spherically bent crystal analyzers (bending radius of 1 m) and an avalanche photodiode arranged in a vertical point-to-point Rowland circle geometry [25]. The HERFD-XAS data are collected at the maximum of the $K\alpha_1$ emission line using Ge(333) analyzers. The XES measurements are performed at the $K\beta$ core-to-core lines ($K\beta'$ and $K\beta_{1,3}$) using Si(440) analyzers and with the incoming excitation set at 6700 eV. For these configurations, the total energy resolutions (convolution of monochromator and spectrometer) are, respectively, ≈1.3 eV and ≈1.0 eV (full width at half maximum). In addition, to exploit the natural linear x-ray dichroism (XLD) arising from the wurtzite hexagonal lattice [26], two geometries are employed: the vertical grazing incidence (VGI) and the horizontal grazing incidence (HGI). The grazing angle fixed at $\approx5°$ permits us to approximate the two configurations, respectively, to $\epsilon \parallel c$ and $\epsilon \perp c$, where ϵ is the polarization vector and c is the wurtzite c axis that corresponds to the sample's surface normal. The number of acquired spectra and the integration time per energy point are chosen in order to reach an edge jump of $\approx10^6$ total counts per spectrum on each specimen. This permits us to obtain the same statistics for all samples. The HERFD- and TFY-mode spectra are collected in the near-edge and extended regions (XANES and EXAFS) for the whole series.

Theoretical calculations are performed to support the analysis of the experimental XANES and EXAFS data. In order to simulate the $Al_xGa_{1-x}N$:Mn series, seven wurtzite supercells (SC), $3a \times 3b \times 2c$ (72 atoms), are built using the program VESTA [27], with Al concentrations corresponding to those found experimentally, as reported in Table I. The experimental lattice parameters established from XRD measurements are employed for the SC, while the wurtzite u parameter is chosen to the average value of $u_{avg} = 0.38$ from Ref. [28]. To simulate the Mn incorporation in the $Al_xGa_{1-x}N$ lattice the following defect configurations are taken into account for one Mn atom as (1) substitutional of Ga or Al (Mn_S); (2) interstitial in the tetrahedral (Mn_{IT}) or octrahedral (Mn_{IO}) sites with Wyckoff positions (2/3, 1/3, u/2) and (0, 0, u/2), respectively. This corresponds to a Mn concentration of $\approx1\%$.

The lattice parameters and atomic positions of the SC are additionally relaxed by means of DFT using the QUANTUM-ESPRESSO package [29]. The first-principles spin-polarized calculations are performed using a plane-wave basis and the projector augmented wave (PAW) method [30]. The exchange correlation energy is described by the Perdew-Burke-Ernzerhof parametrization within the generalized gradient approximation (PBE-GGA) [31]. The Hubbard correction (DFT-GGA+U framework) is applied to Mn with U parameter equal to 3.9 eV [32]. The plane-waves cutoff energy is set to 60 Ry to ensure convergence and the irreducible Brillouin zone is sampled with the Monkhorst-Pack scheme [33] using a $4\times4\times4$ k-point mesh. For each Al concentration (x), the formation energies of Mn impurities substituting Ga or Al ($Mn_{Ga,Al}$) in $Al_xGa_{1-x}N$ (AlGaN) are calculated through $E_f[Mn_{Ga,Al}] = E[Mn_{Ga,Al}] + E[AlGaN] - \mu_{Mn} + \mu_{Ga,Al}$, where $E[Mn_{Ga,Al}]$ and $E[AlGaN]$ are the total energies of $Al_xGa_{1-x}N$:Mn and undoped $Al_xGa_{1-x}N$, respectively. μ_{Mn}, μ_{Ga}, and μ_{Al} are the atom chemical potentials obtained from bulk α-Mn, α-Ga, and Al, respectively.

The Mn K-edge XANES and EXAFS spectra are simulated within the real-space Green's function formalism employing the FDMNES [34] and FEFF9 [35] codes, respectively. The muffin-tin potentials and the Hedin-Lunqvist approximation [36] for the exchange-correlation component are used. The calculations are performed using the DFT-relaxed SC, rescaled to the experimental lattice parameters as input structures. The cluster radius for the spectra is set to 10 Å, while the self-consistent field (SCF) loop is swept within a radius of 6 Å. For the comparison with the experiment, the XANES spectra are consequently convoluted with a Lorentzian function with an energy-dependent arctangent-like width, $\Gamma(E)$ [34]. This model correctly accounts for the core-hole and the photoelectron mean-free-path broadening. The best agreement with the experimental data is found going from $\Gamma_{min} = 0.5$ eV to $\Gamma_{max} = 4.0$ eV. A second convolution with a Gaussian function of constant width (0.9 eV) is also applied to take into account the experimental broadening. These parameters, below the core-hole lifetime, are in line with the expected sharpening effect due to the high resolution detection [37]. The EXAFS signal is extracted from the absorption spectra via the VIPER code [38], using a smoothing spline algorithm and selecting the edge energy E_0 at the maximum of the derivative peak corresponding to the typical shoulder after the pre-edge features. The EXAFS quantitative analysis, which is based on scattering paths expansion, Fourier transform and least-squares fits, is performed with the IFEFFIT [39,40] software. The EXAFS Debye-Waller factors (DWF) for the multiple scattering paths are modeled as the sum of the DWF of single scattering paths plus a Debye model with room temperature (300 K) target and a Debye temperature of 600 K [41]. In both XANES and EXAFS simulations, the polarization effects [26] are correctly included.

III. RESULTS AND DISCUSSION

As a first step, we determine the Al content from the strain analysis on the XRD data. The XRD spectra of the symmetric (004) reflection over the whole series are reported in the top panel of Fig. 1. In the θ-2θ scans for 2θ values between 30° and 80° on all considered samples, only reflections from the sapphire substrate (not shown), from the GaN buffer, and from the Al$_x$Ga$_{1-x}$N layers are detectable, with no indication of secondary phases. From the position of the Al$_x$Ga$_{1-x}$N peak it is possible to deduce the Al$_x$Ga$_{1-x}$N c parameter. In order to gain insight into the Al content in the films, maps of the ($\bar{1}$015) asymmetric reflection have been acquired for the whole series and are shown in the bottom panels of Fig. 1 for the films containing 12% and 40% Al. The strain state of the Al$_x$Ga$_{1-x}$N layer is deduced from the relative position of the ($\bar{1}$015) reflection of GaN and Al$_x$Ga$_{1-x}$N, and the a and c lattice parameters are obtained from the Q_x and Q_z coordinates of the Al$_x$Ga$_{1-x}$N ($\bar{1}$015) reflection, upon a 2D Gaussian fit. To extract the Al concentration, we consider a linear variation of the lattice parameters between GaN and Al$_x$Ga$_{1-x}$N as a function of the Al concentration according to Vegard's law [42] for the relaxed structures. For the strained samples, the compressibility of Al$_x$Ga$_{1-x}$N through the Poisson coefficient is taken into account. It is important to remark that, in the set of samples studied, the layer is either fully strained (#A to #C) or
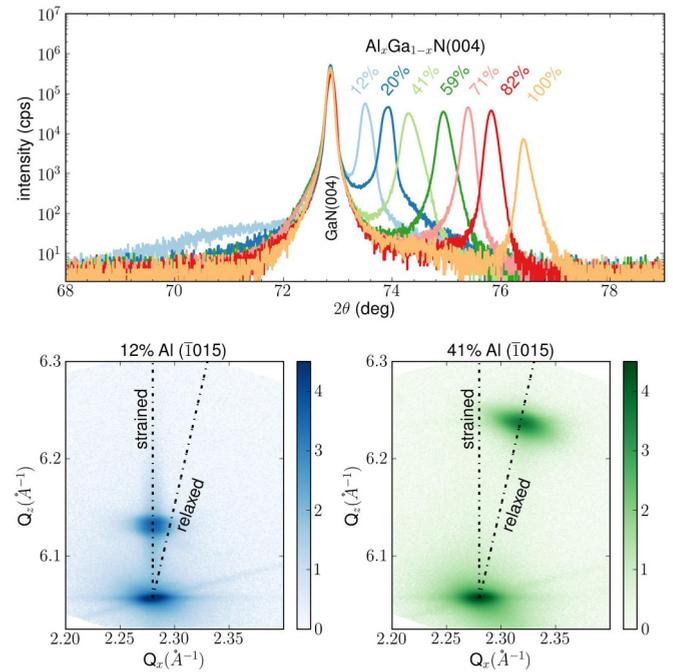
FIG. 1. (Color online) XRD: (top panel) evolution of the GaN and Al$_x$Ga$_{1-x}$N (004) peak position over the whole series; (bottom panels) maps of the ($\bar{1}$015) asymmetric reflection of GaN and Al$_x$Ga$_{1-x}$N measured for Al$_x$Ga$_{1-x}$N:Mn with 12% and 41% Al, respectively.

fully relaxed (#D to #H) where the full relaxation is likely to be due to cracks crossing the layer down to the interface with GaN. The Al concentrations obtained from XRD—as summarized in Table I—are consistent within 1% error with those measured by EDS. The Al$_x$Ga$_{1-x}$N experimental lattice parameters are reported in Table II. The computed lattice parameters closely follow Vegard's law in accord with previous works based on full-potential augmented plane wave method calculations [43]. Nevertheless, the computed lattice parameters overestimate the experimental values by $\approx$1%. This is explained by the strong dependence of DFT on the level of theory employed. For this

TABLE II. Lattice parameters and strain state found experimentally with XRD. The error bar on the last digit is reported in parenthesis. It corresponds to the error propagation from the full width at half maximum ($\approx$2.35 σ) of the fitted two-dimensional Gaussian peak; that is, $\pm$0.01 Å and $\pm$0.004 Å for a and c, respectively.

Sample	x (%)	a (Å)	c (Å)	Strain state
#A	0	3.18(1)	5.187(4)	strained
#B	12	3.18(1)	5.148(4)	strained
#C	20	3.18(1)	5.123(4)	strained
#D	41	3.16(1)	5.100(4)	relaxed
#E	59	3.14(1)	5.063(4)	relaxed
#F	71	3.13(1)	5.038(4)	relaxed
#G	82	3.12(1)	5.014(4)	relaxed
#H	100	3.11(1)	4.980(4)	relaxed
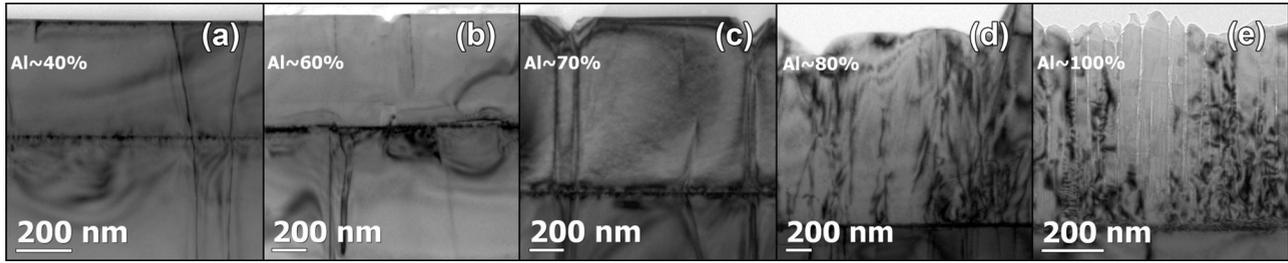
FIG. 2. TEM micrographs of Al_xGa_{1-x}N:Mn layers with (a) 41%, (b) 59%, (c) 71%, (d) 82%, and (e) 100% (samples #D, #E, #F, #G, and #H in Table I).

reason, we force in the DFT-relaxed SC the experimental lattice parameters.

We investigate via DFT also the formation energies upon relaxation for the incorporation of Mn in Al_xGa_{1-x}N. First of all, we study the total energies of the Al_xGa_{1-x}N alloy without Mn with respect to atomic-scale composition fluctuations. This permits us to understand whether the alloy behaves locally as an ordering of GaN and AlN separate unit cells or there is a random distribution of Al/Ga atoms among the cation positions in the SC. For the intermediate Al concentrations $x = 0.25$, 0.5, and 0.75, we compare the total energies for several structures with random position of Al and Ga atoms in cation sites. This means that, for a given intermediate Al concentration—that is, for a given number of Al atoms in the SC—we randomly change the position of Al/Ga atoms in cation sites and calculate the total energy of each configuration. We find that the total energies of those configurations for each Al concentration do not differ by more than 50 meV. From this result, we conclude that the Al_xGa_{1-x}N alloy has Al and Ga cations in random positions for all concentrations of the constituents. The second step consists of investigating the formation energies upon incorporation of Mn at substitutional and interstitial sites. For the substitutional site, we assume that for $x \leqslant 0.5$ Mn substitutes mostly Ga sites, whereas for $x > 0.5$ Mn ions replace Al positions. It is found that Mn_S^{Ga} ($x \leqslant 0.5$) has a constant formation energy of 3.5 eV, while for Mn_S^{Al} ($x > 0.5$) an abrupt increase in the formation energy to 5.5 eV is obtained. This result indicates that, in terms of formation energy, Mn tends to substitute Ga atoms rather than Al ones, challenging the epitaxy of high quality AlN:Mn. On the other hand, this does not take into account the surface energies that play a crucial role during growth. For the interstitial sites (tetrahedral, Mn_{IT}, and octahedral, Mn_{IO}), we find always formation energies higher than the one of Mn_S. Upon relaxation, Mn_{IO} remains at its nominal

site, with a formation energy increasing linearly with x, from 6.5 eV ($x = 0$) to 9.25 eV ($x = 1$). On the other hand, Mn_{IT} is rather unstable and tends to move toward Mn_{IO}; its formation energy is ≈ 8.25 eV, regardless of x. These results show that the substitutional incorporation of Mn in Al_xGa_{1-x}N is favored, as confirmed by the experimental data reported in the following.

According to the TEM micrographs shown in Fig. 2, the layers are structurally homogeneous for Al concentrations up to 82%. Moreover, EDS spot sampling and line scans (not shown) confirm that the layers are chemically homogeneous. In contrast to the layer-by-layer growth of Al_xGa_{1-x}N:Mn up to Al concentrations as high as 82% shown in Figs. 2(a)–2(d), the columnar structure of the AlN:Mn sample is evidenced in Fig. 2(e). The Al_xGa_{1-x}N:Mn layer with 82% Al is still structurally coherent with the GaN buffer layer, but at the boundary between 2D and 3D growth. The homogeneous structure of the Al_xGa_{1-x}N:Mn layers with Al (a) 41%, (b) 59%, (c) 71%, and (d) 82% is evidenced by the HRTEM images taken close to the [11$\bar{2}$0] zone axis and reported in Fig. 3. According to a fast Fourier transform (FFT) analysis, there is no compositional ordering or modulation of the Al concentration, in contrast to what was reported previously for Al_xGa_{1-x}N layers without Mn [44]. In the HRTEM image of Fig. 3(e) the boundary between two columnar structures in the AlN:Mn layer is reported. Here, the arrow a indicates a gap between the two columns, while arrow b points to planar defects in the basal plane formed in the AlN:Mn layer.

Having established the lattice parameters (long-range structure), strain state, and Al concentration with XRD, and the microstructure of the layers by means of TEM, we apply XAS and XES to probe the local atomic and electronic structure around Mn impurities. The approach employed here follows a well established method applied in previous studies of GaN:Mn [12,45], GaN:Mn,Mg [46], and related systems such as ZnO:Mn [47] and GaN:Sc [48]. Supported by the
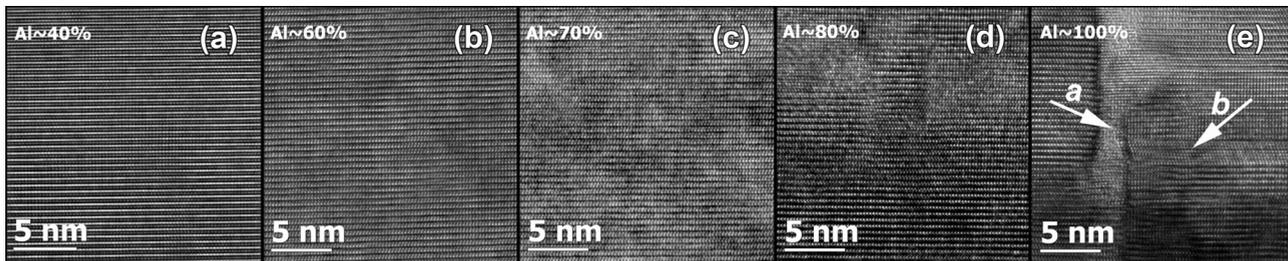
FIG. 3. HRTEM images of Al_xGa_{1-x}N:Mn layers (a) 41%, (b) 59%, (c) 71%, (d) 82%, and (e) 100% (samples #D, #E, #F, #G, and #H in Table I).
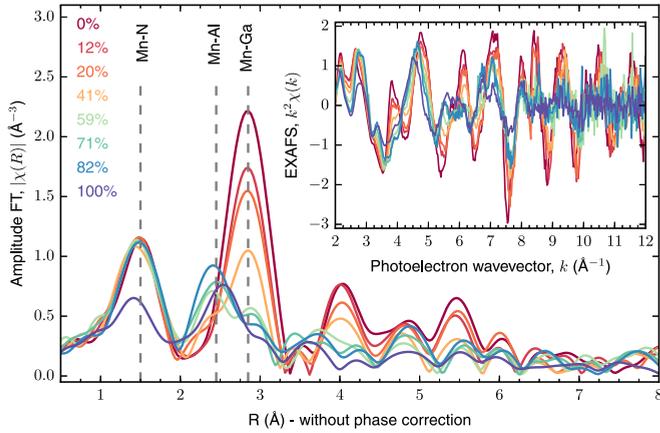
FIG. 4. (Color online) Amplitude of the Fourier transform (FT) of the k^2-weighted EXAFS signal, $\chi(k)$—shown in the inset—for all the samples (identified by Al%), collected in VGI geometry. The FT is performed using a Hanning window ($dk = 1$) in the k range 2.5–9.5 Å^{-1}. The three vertical dashed lines show the nominal position of the Mn-N, Mn-Al, and Mn-Ga next-nearest-neighbors' bond distances in R space (without phase correction; that is, the shown R scale does not correspond to the absolute bond distances).

complementary spectroscopic techniques EXAFS, XANES, XLD, and XES, we demonstrate that at least 90% of the Mn atoms incorporate into the Al$_x$Ga$_{1-x}$N lattice as random substitutional impurities at the cation site (Mn$_S$) with a local spin moment $S = 2$ in all the samples containing up to 82% of Al.

The EXAFS technique is a well established powerful tool for the local structure characterization of doped semiconductors [49,50]. The system under study is very challenging for the conventional Fourier transform (FT) quantitative analysis of the EXAFS data. In fact, not only is the lattice distorted locally by the introduction of the Mn dopant (similarly to, e.g., GaN:Mn or AlN:Mn), but also the alloying effect due to the ternary compound Al$_x$Ga$_{1-x}$N strongly affects the resulting spectra that represent an average pair distribution function around the Mn atoms. As shown in Fig. 4, there is an evolution of the EXAFS signal with the Al concentration. The main changes are visible in the k region 2.5–9.5 Å^{-1}, which is especially sensitive to the Mn next-nearest-neighbors average configuration. In particular, the evolution of the spectral features at ≈ 4 Å^{-1} and at ≈ 6 Å^{-1} may be understood by taking into account the destructive interference of the out-of-phase Mn-Ga and Mn-Al scattering paths in the cation-cation coordination shells. This effect is evidenced by taking the amplitude of the FT in the range of interest. The first peak, which represents the Mn-N bond distance, is substantially constant up to 82% Al. The second and third main peaks, corresponding to Mn-Al and Mn-Ga coordination shells, respectively, show a continuous evolution with increasing Al concentration. In a simple qualitative analysis and in first approximation, the intensity and position of these peaks can be ascribed to the coordination number and average bond distance of the corresponding scattering paths, respectively. The fact that the Mn-N peak is constant up to 82% Al points to a Mn$_S$ well ordered defect, while the reduction (increase) in amplitude of the Mn-Ga (Mn-Al) peak is related to the alloying
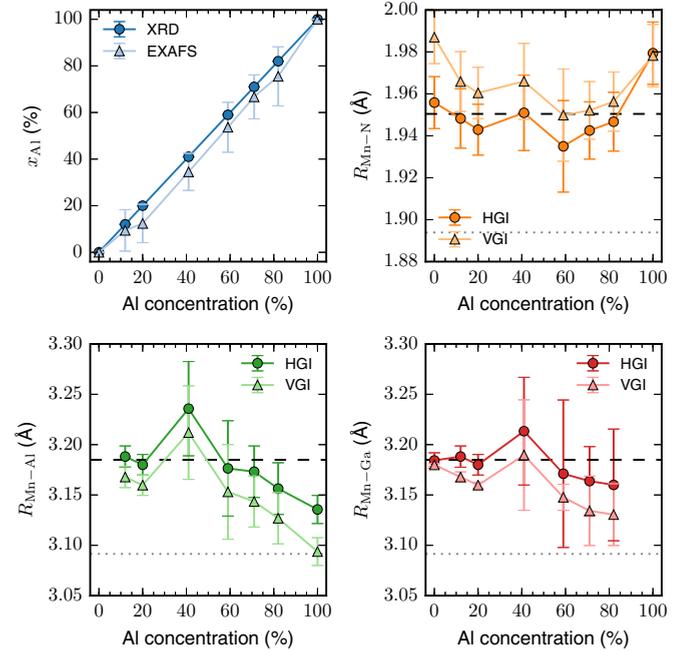
FIG. 5. (Color online) Results of the EXAFS quantitative analysis for x_{Al}, R_{Mn-N}, R_{Mn-Al}, and R_{Mn-Ga} variables (as reported in Table III). The horizontal lines are the corresponding average bond distances for GaN (dashed) and AlN (dotted).

effect and permits us to quantify the local Al concentration and bond distances. Moreover, the strong overall amplitude reduction for the AlN:Mn sample (100% Al) is the hint of a locally disordered environment and is in line with the disordered micro/nano-structure previously revealed by TEM measurements.

A quantitative analysis via a least-squares fit of the EXAFS data is then performed. Due to the complexity of the system under investigation and in order to keep the correlation between the fitted variables as low as possible, a model with a minimum set of parameters to describe the whole Al concentration range is found. This corresponds to the best fitting model and consists of a Mn$_S$ defect in Al$_x$Ga$_{1-x}$N expanded in three sets of single scattering paths: Mn-N, Mn-Al, and Mn-Ga, corresponding to the first three coordination shells. For each sample, the fit is performed in R space, limited to the 1–3.5 Å range. Both VGI and HGI data sets (weighted by the noise level) are included in a single fit in order to correctly account for the polarization effects. This permits us to report the average bond distances for the out-of-plane (VGI, parallel to c) and in-plane (HGI, perpendicular to c) atomic configurations. The results are shown in Table III, Fig. 5 and in the Supplemental Material, Fig. S1 [51]. The model is built as follows: the passive electron reduction factor [52], S_0^2, is fixed to the calculated value of 0.935; the coordination numbers for Mn-N and Mn-Al are fitted, respectively, via the variables x_N and x_{Al}, while the coordination number of the second cation shell is constrained to sum to 12; a common Debye-Waller factor, which accounts for both the structural and thermal disorder, is fitted to σ^2 for all single scattering paths; three variables are employed for the Mn-N, Mn-Al and Mn-Ga average distances, R_{Mn-N}, R_{Mn-Al} and R_{Mn-Ga},

TABLE III. Results of the EXAFS quantitative analysis.

Sample	x_N (%)	x_{Al} (%)	σ^2 (10^{-3} Å^{-2})	R_{Mn-N} VGI (Å)	R_{Mn-N} HGI (Å)	R_{Mn-Al} VGI (Å)	R_{Mn-Al} HGI (Å)	R_{Mn-Ga} VGI (Å)	R_{Mn-Ga} HGI (Å)
#A	89(9)	0	4(2)	1.99(1)	1.96(1)			3.18(1)	3.18(1)
#B	80(13)	10(8)	4(2)	1.97(1)	1.95(1)	3.17(1)	3.18(1)	3.17(1)	3.17(1)
#C	73(10)	12(8)	4(2)	1.96(1)	1.94(1)	3.16(1)	3.18(1)	3.16(1)	3.16(1)
#D	85(14)	35(8)	8(3)	1.97(2)	1.95(2)	3.21(4)	3.23(5)	3.19(5)	3.19(5)
#E	85(16)	54(10)	6(3)	1.95(2)	1.94(2)	3.15(5)	3.18(5)	3.15(1)	3.15(7)
#F	77(18)	67(9)	7(3)	1.95(1)	1.94(1)	3.14(2)	3.17(3)	3.13(3)	3.13(3)
#G	74(18)	76(12)	7(4)	1.96(1)	1.95(1)	3.12(2)	3.15(3)	3.13(3)	3.13(5)
#H	63(9)	100	9(3)	1.98(1)	1.98(1)	3.09(1)	3.14(1)		

respectively, with a common expansion/contraction factor in the two orthogonal directions (VGI and HGI); a common variable is fitted also for the shift of the edge energy, ΔE_0. This model permits us to keep the numerical correlation between the variables below a 50% level. The R factor of the fits ranges from 0.009 to 0.04, affecting the propagated error bars, as reported in Table III. Several additional fitting models have been tested, either increasing the number of fitted variables or introducing additional scattering paths from other defects, as Mn interstitials (Mn_{IO} and Mn_{IT}). In all cases those models do not pass an F test [53,54], meaning that the improvement in the fit quality is not statistically relevant. The EXAFS quantitative analysis indicates that the majority of Mn atoms is in a Mn_S configuration. On the other hand, the fitted percentage of x_N does not correspond exactly to the percentage of Mn_S in the samples. In fact, the absolute value of this variable, which represents the coordination of the first coordination shell (Mn-4N tetrahedron), is affected by the numerical correlation with σ^2 and by the presence of nitrogen vacancies, as found in similar samples [55]. For this reason, we rely on the results of the XLD analysis, which is much more sensitive to the symmetry of the crystal, for determining the level of Mn_S in the samples. Nevertheless, a strong k-independent amplitude reduction of the EXAFS signal is obtained for the AlN:Mn sample (#H). As shown by the TEM micrographs, this sample has a columnar structure, thus the amplitude reduction is attributed to an increased local disorder, as was demonstrated by EXAFS simulations combined with molecular dynamics calculations for Mn nanocolumns in Ge:Mn [56]. The second percentage parameter, x_{Al}, is extracted from the fitted coordination number of the second coordination shell, keeping the constraint of 12 total neighbors (Ga/Al) dictated by the wurtzite structure. The results follow a linear dependence and match, within the error bars, with the Al concentration found by XRD. Furthermore, it is found that the average Mn-N bond distance is larger than those of Ga-N or Al-N and is not affected by the Al doping, while Mn-Al and Mn-Ga show a contraction going from GaN:Mn to AlN:Mn, as expected by the reduction of the lattice parameters. This implies that the lattice distortion introduced by the Mn incorporation is local and mainly limited to the first coordination shell. In order to further confirm the local structural description obtained via EXAFS analysis, the XANES region is investigated through *ab initio*

simulations. In Fig. 6 the normalized $K\alpha_1$ HERFD-XANES spectra are shown together with their relative simulations (using the FDMNES [34] code) for the HGI and VGI geometries. The HERFD-XANES spectra correspond to a diagonal cut in the 2D resonant inelastic x-ray scattering (RIXS) plane [37] and can be approximated to standard XANES spectra only in the region above the pre-edge, where the spectral features arise from electric dipole transitions from $1s$ to $4p$ empty states of the absorbing atoms (Mn). This energy range can be described in an approximate way by multiple scattering theory employing simple muffin-tin potentials [57] within a one-electron approach, i.e., the level of theory employed for the simulated spectra shown in this study. The spectral features present in the pre-edge region of the HERFD-XANES spectra cannot be fully described by the level of theory employed here, and a quantitative analysis requires us to account for the full RIXS plane, not only for line cuts [37]. Nevertheless, the presence of an intense pre-edge peak in the K-edge
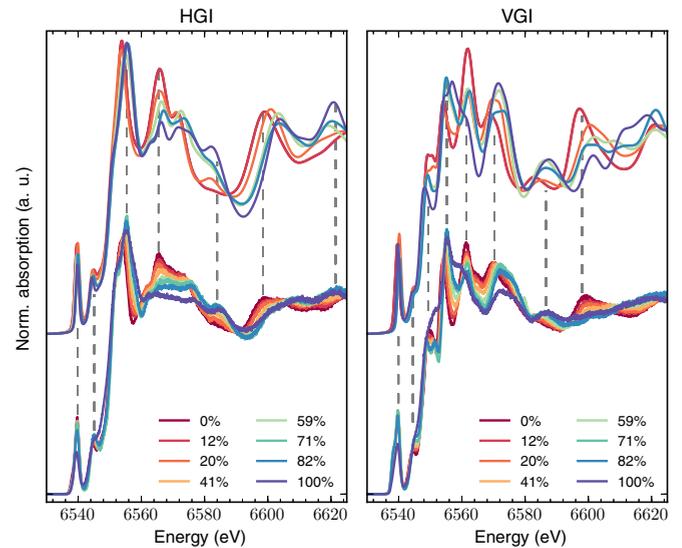
FIG. 6. (Color online) Normalized $K\alpha_1$ HERFD-XANES spectra (bottom) for the $Al_xGa_{1-x}N$:Mn series with the corresponding simulations (top) for HGI (left panel) and VGI (right panel) geometries. The simulations correspond to a Mn in a DFT-relaxed substitutional site (Wyckoff 2b). The vertical dashed lines are guides to the eye of the main spectral features.

XAS spectra of 3d transition metals is the fingerprint of tetrahedral (T_D) symmetry [58,59], due to allowed electric dipole transitions to the p character of the t_2 spin-polarized 3d states. The spectral features present in the XANES region do not correlate straightforwardly with a given coordination shell or scattering species, but are the result of full multiple scattering paths. This induces an enhanced sensitivity to the geometry around the absorber. On the other hand, this also makes it challenging to quantitatively model the XANES via *ab initio* methods. As shown in Fig. 6, all the spectral features and the trend with increasing Al concentration are reproduced by the simulations using a substitutional model based on the DFT-relaxed SC, rescaled to the experimental lattice parameters. To better evaluate the quality of each simulation, Figs. S2 and S3 in the Supplemental Material [51] show the comparison with experimental spectra for the nominal Wyckoff sites and the DFT-relaxed positions. The defects investigated are Mn$_S$, Mn$_{IT}$, and Mn$_{IO}$ in Al$_x$Ga$_{1-x}$N. In order to get more quantitative results, a linear combination fit (LCF) analysis of the XANES spectra is performed. The constraints imposed are the following: the presence of the Mn$_S$ phase; the number of components is limited to two (one substitutional and one interstitial); and an energy shift for the interstitial phase is allowed (fitted). All combinations among the four interstitial cells are performed and the fits are ranked by χ^2. In all samples/geometries it is found that the Mn$_S$ phase is >80% and the complementary phase is the nonrelaxed Mn$_{IT}$ defect. On the other hand, the χ^2 values of the best fits do not pass a statistical test (F test), meaning that the increase in the fit quality is not relevant. This confirms what was previously found by EXAFS and the formation energies results of the DFT: that is, that the Mn$_{IT}$ defect in Al$_x$Ga$_{1-x}$N is not stable and has a high formation energy. A more quantitative analysis to establish the percentage of Mn atoms incorporating as substitutional defects in the host matrix is obtained by studying the XLD spectra. It is established that XLD is extremely sensitive to the symmetry of non-cubic sites [26] and it was shown to be a powerful tool to determine the quality of substitutional inclusions in dilute magnetic semiconductors [60]. The XLD spectra for the studied samples are reported in Fig. 7 and are obtained from the difference between the HERFD-XANES spectra in VGI and HGI geometries. The amplitude of the XLD main oscillation at the edge position highlighted in Fig. 7 is taken as a figure of merit for Mn$_S$. In fact, the maximum XLD amplitude would be obtained for 100% Mn$_S$ dilute in a perfect Al$_x$Ga$_{1-x}$N lattice. The Mn$_{IT}$ interstitial shows an XLD signal too; however, it is not in phase with the Mn$_S$ XLD signal and the resulting XLD amplitude in the region of interest is reduced. As a reference for the 100% case, we arbitrarily rescale the experimental XLD amplitudes to the XLD amplitude at the Ga K edge of a GaN:Mn layer from Ref. [61]. The results are reported in the inset to Fig. 7. The increasing values of the Mn$_S$ percentage for Al $\leqslant$82% are due to the accuracy of the normalization procedure employed. In fact, a more accurate method would require us to rescale the Mn K-edge XLD amplitudes to the Ga K-edge (or Al K-edge) XLD amplitude measured for each sample in the same experimental conditions. On the other hand, the systematic errors are estimated to be within a ±10% bandwidth. The dramatically low Mn$_S$ value for
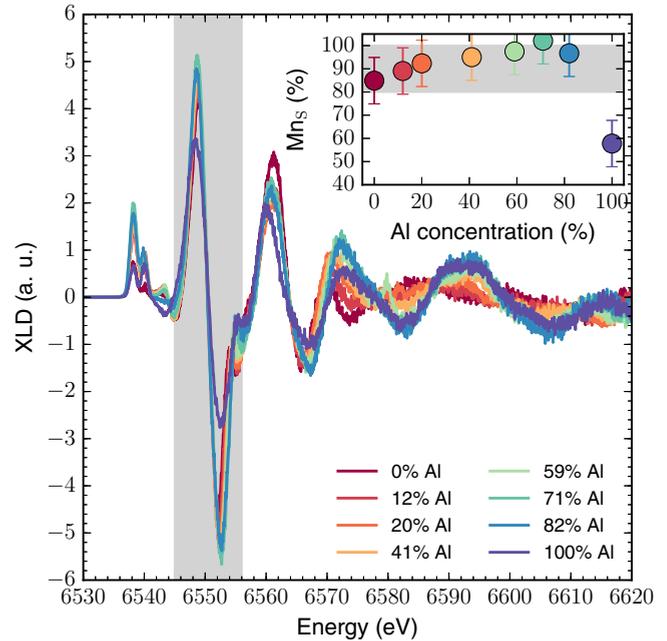
FIG. 7. (Color online) XLD signal for the Al$_x$Ga$_{1-x}$N:Mn series. The amplitude in the highlighted region is taken as a figure of merit for Mn$_S$. Inset: quantitative analysis of the results.

AlN:Mn can be safely attributed to an actual reduction of Mn$_S$ in this sample. As final point we discuss the Mn valence state inferred from the integral of the absolute difference of the Kβ XES data (integrated absolute difference: IAD analysis [37]). This method is preferred over the one employing the position of the main absorption edge for the possibility it gives to quantitatively follow the evolution of the effective spin moment on Mn (S_{eff}) as a function of a given parameter and to directly compare the results with DFT calculations [37]. The total magnetic moment per unit cell calculated with DFT is in all cases $4\mu_B$ and corresponds to $S_{eff} \approx 2.0$, as found in the frame of a Bader partitioning scheme [37]. This result is confirmed experimentally, as reported in Fig. 8. The Mn valence state is constant within the error bar for the whole series, with the exception of the AlN:Mn sample, as expected and supporting all previous results.

IV. CONCLUSIONS AND OUTLOOK

We have carried out an extensive study of epitaxial Al$_x$Ga$_{1-x}$N:Mn on a series of samples with Al concentration up to 100%. By XRD we have found that the Al content in the layers matches—over the sample series—the one expected from growth conditions. The lattice parameters as a function of the Al concentration are also obtained by XRD. The DFT computations on the formation energy for the incorporation of Al in a GaN matrix let us to conclude that Al and Ga are randomly distributed into the lattice, and in Al$_x$Ga$_{1-x}$N:Mn the Mn ions have the tendency to preferentially substitute for Ga. The formation of Mn interstitial defects is not favored. A coherent growth without local aggregation or precipitation is obtained for Al$_x$Ga$_{1-x}$N:Mn with Al concentrations up to 82%, confirming the surfactant role of Mn already reported [21]. Synchrotron radiation XAS has been employed to probe
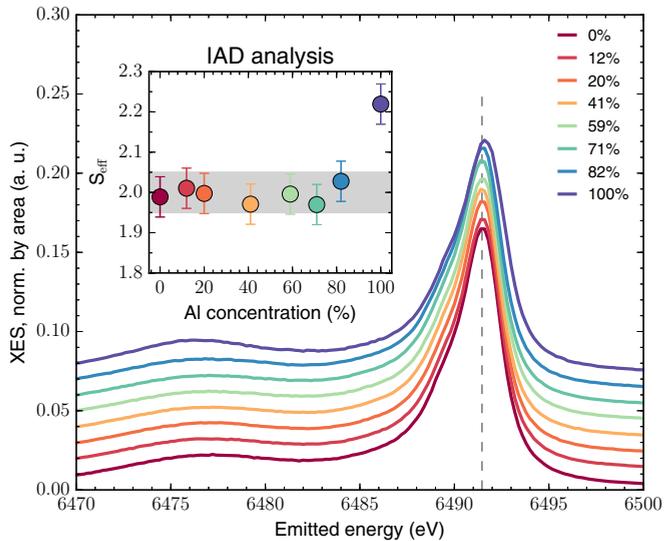
FIG. 8. (Color online) Mn $K\beta$ XES data over the whole series of samples. Inset: relative IAD analysis. The vertical dashed line is a guide to the eye.

layers. An IAD analysis of the XES data allows to determine the valence state of Mn as constant up to an Al concentration of 82%. Due to the reduced lattice parameters with respect to, e.g., GaN:Mn, enhanced hybridization of the orbitals can be expected in $Al_xGa_{1-x}N$:Mn, making it a material system worth investigating in view of spintronic functionalities. Moreover, this work paves the way to the understanding and control of the role played by Mn in particular and transition metals in general on the structure and properties of the alloys $Al_xGa_{1-x}N$:TM. Significantly, the incorporation of Mn has been found to promote the growth of $Al_xGa_{1-x}N$ on GaN, to defer the relaxation of the layers, and to increase the critical thickness also for Al concentrations up to 82%, with remarkable potential effects on the fabrication of, e.g., distributed Bragg mirrors for group-III-nitride-based optoelectronic devices.

ACKNOWLEDGMENTS

the local atomic and electronic structure of Mn. From EXAFS, XANES, and XLD it is found that the majority of the Mn ions are dilute, i.e., homogeneously distributed over the doped

[1] H. Morcoç, *Handbook of Nitride Semiconductors and Devices, Volume 3, GaN-based Optical and Electronic Devices* (Wiley-VCH, Weinheim, 2008).

[2] R. Gutt, T. Passow, M. Kunzer, W. Pletschen, L. Kirste, K. Forghani, F. Scholz, K. Köhler, and J. Wagner, Appl. Phys. Exp. **5**, 032101 (2012).

[3] H. Yoshida, Y. Yamashita, M. Kuwabara, and H. Kan, Nat. Photon. **2**, 551 (2008).

[4] S. Nakamura and S. F. Chichibu, *Introduction to Nitride Semiconductor Blue Lasers and Light Emitting Diodes* (CRC Press, Boca Raton, FL, 2000), p. 386.

[5] M. Shur, Solid. State. Electron. **42**, 2131 (1998).

[6] U. Mishra and P. Parikh, Proc. IEEE **90**, 1022 (2002).

[7] T. Dietl and H. Ohno, Rev. Mod. Phys. **86**, 187 (2014).

[8] T. Kondo, S. Kuwabara, H. Owa, and H. Munekata, J. Cryst. Growth **237-239**, 1353 (2002).

[9] G. Martinez-Criado, A. Somogyi, S. Ramos, J. Campo, R. Tucoulou, M. Salome, J. Susini, M. Hermann, M. Eickhoff, and M. Stutzmann, Appl. Phys. Lett. **86**, 131927 (2005).

[10] E. Sarigiannidou, F. Wilhelm, E. Monroy, R. M. Galera, E. Bellet-Amalric, A. Rogalev, J. Goulon, J. Cibert, and H. Mariette, Phys. Rev. B **74**, 041306(R) (2006).

[11] A. A. Freeman, K. W. Edmonds, N. R. S. Farley, S. V. Novikov, R. P. Campion, C. T. Foxon, B. L. Gallagher, E. Sarigiannidou, and G. van der Laan, Phys. Rev. B **76**, 081201(R) (2007).

[12] A. Bonanni, M. Sawicki, T. Devillers, W. Stefanowicz, B. Faina, T. Li, T. E. Winkler, D. Sztenkiel, A. Navarro-Quezada, M. Rovezzi, R. Jakieła, A. Grois, M. Wegscheider, W. Jantsch,

J. Suffczyński, F. D'Acapito, A. Meingast, G. Kothleitner, and T. Dietl, Phys. Rev. B **84**, 035206 (2011).

[13] M. Sawicki, T. Devillers, S. Gałęski, C. Simserides, S. Dobkowska, B. Faina, A. Grois, A. Navarro-Quezada, K. N. Trohidou, J. A. Majewski, T. Dietl, and A. Bonanni, Phys. Rev. B **85**, 205204 (2012).

[14] S. Stefanowicz, G. Kunert, C. Simserides, J. A. Majewski, W. Stefanowicz, C. Kruse, S. Figge, T. Li, R. Jakieła, K. N. Trohidou, A. Bonanni, D. Hommel, M. Sawicki, and T. Dietl, Phys. Rev. B **88**, 081201(R) (2013).

[15] G. Kunert, S. Dobkowska, T. Li, H. Reuther, C. Kruse, S. Figge, R. Jakiela, A. Bonanni, J. Grenzer, W. Stefanowicz, J. von Borany, M. Sawicki, T. Dietl, and D. Hommel, Appl. Phys. Lett. **101**, 022413 (2012).

[16] A. Y. Polyakov, N. B. Smirnov, A. V. Govorkov, S. J. Pearton, R. M. Frazier, G. T. Thaler, C. R. Abernathy, and J. M. Zavada, Semicond. Sci. Technol. **19**, 1169 (2004).

[17] A. Y. Polyakov, N. B. Smirnov, A. V. Govorkov, R. M. Frazier, G. T. Thaler, C. R. Abernathy, S. J. Pearton, J. M. Zavada, and R. G. Wilson, J. Electron. Mater. **33**, 384 (2004).

[18] M. L. Reed, E. A. Berkman, M. J. Reed, F. E. Arkun, T. Chikyow, S. M. Bedair, J. M. Zavada, and N. A. El-Masry, Mater. Res. Soc. Proc. **798**, Y8.6 (2011).

[19] R. M. Frazier, G. T. Thaler, C. R. Abernathy, S. J. Pearton, M. L. Nakarmi, K. B. Nam, J. Y. Lin, H. X. Jiang, J. Kelly, R. Rairigh, A. F. Hebard, J. M. Zavada, and R. G. Wilson, J. Appl. Phys. **94**, 4956 (2003).

[20] H.-K. Seong, Y. Lee, J.-Y. Kim, Y.-K. Byeun, K.-S. Han, J.-G. Park, and H.-J. Choi, Adv. Mater. **18**, 3019 (2006).

[21] T. Devillers, L. Tian, R. Adhikari, G. Capuzzo, and A. Bonanni, Cryst. Growth Des. **15**, 587 (2015).

[22] A. Bonanni, D. Stifter, A. Montaigne-Ramil, K. Schmidegg, K. Hingerl, and H. Sitter, J. Cryst. Growth **248**, 211 (2003).

[23] S. Peters, T. Schmidtling, T. Trepk, U. W. Pohl, J.-T. Zettler, and W. Richter, J. Appl. Phys. **88**, 4085 (2000).

[24] M. A. Moram and M. E. Vickers, Rep. Prog. Phys. **72**, 036502 (2009).

[25] P. Glatzel, T.-C. Weng, K. Kvashnina, J. Swarbrick, M. Sikora, E. Gallo, N. Smolentsev, and R. A. Mori, J. Electron Spectros. Relat. Phenom. **188**, 17 (2013).

[26] C. Brouder, J. Phys. Condens. Matter **2**, 701 (1990).

[27] K. Momma and F. Izumi, J. Appl. Crystallogr. **44**, 1272 (2011).

[28] W. Paszkowicz, S. Podsiadło, and R. Minikayev, J. Alloys Compd. **382**, 100 (2004).

[29] P. Giannozzi, S. Baroni, N. Bonini, M. Calandra, R. Car, C. Cavazzoni, D. Ceresoli, G. L. Chiarotti, M. Cococcioni, I. Dabo, A. Dal Corso, S. de Gironcoli, S. Fabris, G. Fratesi, R. Gebauer, U. Gerstmann, C. Gougoussis, A. Kokalj, M. Lazzeri, L. Martin-Samos, N. Marzari, F. Mauri, R. Mazzarello, S. Paolini, A. Pasquarello, L. Paulatto, C. Sbraccia, S. Scandolo, G. Sclauzero, A. P. Seitsonen, A. Smogunov, P. Umari, and R. M. Wentzcovitch, J. Phys. Condens. Matter **21**, 395502 (2009).

[30] P. E. Blöchl, Phys. Rev. B **50**, 17953 (1994).

[31] J. P. Perdew, K. Burke, and M. Ernzerhof, Phys. Rev. Lett. **77**, 3865 (1996).

[32] N. Gonzalez Szwacki, J. Majewski, and T. Dietl, Phys. Rev. B **83**, 184417 (2011).

[33] H. J. Monkhorst and J. D. Pack, Phys. Rev. B **13**, 5188 (1976).

[34] O. Bunău and Y. Joly, J. Phys. Condens. Matter **21**, 345501 (2009).

[35] J. J. Rehr, J. J. Kas, F. D. Vila, M. P. Prange, and K. Jorissen, Phys. Chem. Chem. Phys. **12**, 5503 (2010).

[36] L. Hedin and B. I. Lundqvist, J. Phys. C: Solid State Phys. **4**, 2064 (1971).

[37] M. Rovezzi and P. Glatzel, Semicond. Sci. Technol. **29**, 023002 (2014).

[38] K. V. Klementev, J. Phys. D: Appl. Phys. **34**, 209 (2001).

[39] M. Newville, J. Synchrotron Radiat. **8**, 322 (2001).

[40] B. Ravel and M. Newville, J. Synchrotron Radiat. **12**, 537 (2005).

[41] R. Pässler, J. Appl. Phys. **101**, 93513 (2007).

[42] A. R. Denton and N. W. Ashcroft, Phys. Rev. A **43**, 3161 (1991).

[43] Z. Dridi, B. Bouhafs, and P. Ruterana, Semicond. Sci. Technol. **18**, 850 (2003).

[44] M. Gao, S. T. Bradley, Y. Cao, D. Jena, Y. Lin, S. A. Ringel, J. Hwang, W. J. Schaff, and L. J. Brillson, J. Appl. Phys. **100**, 103512 (2006).

[45] W. Stefanowicz, D. Sztenkiel, B. Faina, A. Grois, M. Rovezzi, T. Devillers, F. D'Acapito, A. Navarro-Quezada, T. Li, R. Jakieła,

M. Sawicki, T. Dietl, and A. Bonanni, Phys. Rev. B **81**, 235210 (2010).

[46] T. Devillers, M. Rovezzi, N. G. Szwacki, S. Dobkowska, W. Stefanowicz, D. Sztenkiel, A. Grois, J. Suffczyński, A. Navarro-Quezada, B. Faina, T. Li, P. Glatzel, F. D'Acapito, R. Jakieła, M. Sawicki, J. A. Majewski, T. Dietl, and A. Bonanni, Sci. Rep. **2**, 722 (2012).

[47] A. A. Guda, N. Smolentsev, M. Rovezzi, E. M. Kaidashev, V. E. Kaydashev, A. N. Kravtsova, V. L. Mazalova, A. P. Chaynikov, E. Weschke, P. Glatzel, and A. V. Soldatov, J. Anal. At. Spectrom. **28**, 1629 (2013).

[48] S. M. Knoll, M. Rovezzi, S. Zhang, T. B. Joyce, and M. A. Moram, J. Phys. Condens. Matter **26**, 225801 (2014).

[49] F. Boscherini, in *Characterization of Semicondctor Heterostructures and Nanostructures*, edited by C. Lamberti (Elsevier, Amsterdam, 2008), Chap. 9, pp. 289–330.

[50] F. D'Acapito, Semicond. Sci. Technol. **26**, 064004 (2011).

[51] See Supplemental Material at http://link.aps.org/supplemental/10.1103/PhysRevB.92.115308 for additional figures on the EXAFS and XANES analysis.

[52] G. G. Li, F. Bridges, and C. H. Booth, Phys. Rev. B **52**, 6332 (1995).

[53] A. Michalowicz, K. Provost, S. Laruelle, A. Mimouni, and G. Vlaic, J. Synchrotron Radiat. **6**, 233 (1999).

[54] L. Downward, C. H. Booth, W. W. Lukens, and F. Bridges, in *X-Ray Absorption Fine Structure - XAFS13: 13th International Conference*, July 2006, Stanford, edited by B. Hedman and P. Pianetta, AIP Conf. Proc. No. 882 (AIP, New York, 2007), pp. 129–131.

[55] E. Piskorska-Hommel, M. J. Winiarski, G. Kunert, I. N. Demchenko, O. D. Roshchupkina, J. Grenzer, J. Falta, D. Hommel, and V. Holý, J. Appl. Phys. **117**, 065702 (2015).

[56] E. Arras, F. Lançon, I. Slipukhina, E. Prestat, M. Rovezzi, S. Tardif, A. Titov, P. Bayle-Guillemaud, F. d'Acapito, A. Barski, V. Favre-Nicolin, M. Jamet, J. Cibert, and P. Pochet, Phys. Rev. B **85**, 115204 (2012).

[57] J. C. Slater, Phys. Rev. **51**, 846 (1937).

[58] T. E. Westre, P. Kennepohl, J. G. DeWitt, B. Hedman, K. O. Hodgson, and E. I. Solomon, J. Am. Chem. Soc. **119**, 6297 (1997).

[59] T. Yamamoto, X-Ray Spectrum. **37**, 572 (2008).

[60] A. Ney, M. Opel, T. C. Kaspar, V. Ney, S. Ye, K. Ollefs, T. Kammermeier, S. Bauer, K.-W. Nielsen, S. T. B. Goennenwein, M. H. Engelhard, S. Zhou, K. Potzger, J. Simon, W. Mader, S. M. Heald, J. C. Cezar, F. Wilhelm, A. Rogalev, R. Gross, and S. A. Chambers, New J. Phys. **12**, 013020 (2010).

[61] F. Wilhelm, E. Sarigiannidou, E. Monroy, A. Rogalev, N. Jaouen, H. Mariette, and J. Goulon, in *Ninth International Conference on Synchrotron Radiation Instrumentation*, 2006, Daegu (Korea), edited by J.-Y. Choi and S. Rah, AIP Conf. Proc. No. 879 (AIP, New York, 2007), pp. 1675–1678.